

# Image Segmentation using Transfer Learning with DeepLabv3 to Facilitate Photogrammetric Limb Scanning

This paper was downloaded from TechRxiv (<https://www.techrxiv.org>).

LICENSE

CC BY 4.0

SUBMISSION DATE / POSTED DATE

10-05-2022 / 16-05-2022

CITATION

Cabrera, Isaac A.; Zhou, Yixuan; Ngo, Eric; Rao, Ramesh R.; Lin, Albert Y. (2022): Image Segmentation using Transfer Learning with DeepLabv3 to Facilitate Photogrammetric Limb Scanning. TechRxiv. Preprint. <https://doi.org/10.36227/techrxiv.19742488.v1>

DOI

[10.36227/techrxiv.19742488.v1](https://doi.org/10.36227/techrxiv.19742488.v1)

# Image Segmentation using Transfer Learning with DeepLabv3 to Facilitate Photogrammetric Limb Scanning

Isaac A. Cabrera, Yixuan Zhou, Eric K. Ngo, Ramesh R. Rao *Fellow, IEEE*,  
Albert Y.M. Lin

**Abstract**—In this paper, we explore the use of deep learning (DL) in conjunction with photogrammetry for scanning amputated limbs. Combining these two technologies can expand the scope of prosthetic telemedicine by facilitating low-cost limb scanning using cell phones. Previous research identified image segmentation as one of the main limitations of using photogrammetry for limb scanning. Based on those limitations, this work sought to answer two main research questions: (1) Can a neural network be trained to identify and segment an amputated limb automatically? (2) Will segmenting 2D limb images using neural networks impact the accuracy of 3D models generated via photogrammetry? To answer the first question, transfer learning was applied to a neural network with the DeepLabv3 architecture. After training, the model was able to successfully identify and segment limb images with an IoU of 79.9%. To answer the second question, the fine-tuned DL model was applied to a dataset of 22 scans comprising 6312 limb images, then 3D models were rendered utilizing Agisoft Metashape. The Mean Absolute Error (MAE) of models rendered from images segmented with DL was  $0.57 \text{ mm} \pm 0.63 \text{ mm}$  when compared to models rendered from ground truth images. These results are important because segmentation with DL makes photogrammetry for limb scanning feasible on a large clinical scale. Future work should focus on generalizing the segmentation model for different types of amputations and imaging conditions.

**Index Terms**—3D Scanning, Deep Learning, Image Segmentation, Photogrammetry, Telemedicine

## I. INTRODUCTION

Rehabilitative care for persons with limb loss is rapidly evolving due to advances in digital healthcare technologies. Novel digital workflows are empowering clinicians with tools for visualizing patient anatomy and physiology, designing custom fitting prostheses via computer aided design (CAD),

Manuscript received May 10, 2022. Funding for this research was provided by the Benbough Foundation, Alfred P. Sloan Foundation, UC San Diego Graduate Division, UCSD Center for Human Frontiers, and the Qualcomm Institute at UCSD.

Isaac A. Cabrera is with the Department of Mechanical and Aerospace Engineering, University of California San Diego, La Jolla, CA 92093, United States (e-mail: iacabrer@eng.ucsd.edu).

Yixuan Zhou and Eric K. Ngo are with the Department of Computer Science and Engineering, University of California San Diego, La Jolla, CA 92093, United States

Ramesh R. Rao and Albert Y.M. Lin are with the California Institute for Telecommunications and Information Technology (Calit2), La Jolla, CA 92093, United States

building assistive devices with computer aided manufacturing (CAM), and tracking patient response in environments such as virtual reality (VR) [1]. Medical imaging technologies are fundamental to every digital workflow because they inform clinicians of limb geometry, surface and/or sub-surface features, plus pathology of amputated limbs [2].

Systematic reviews by [1] and [2] identified photogrammetry as a promising technology for capturing patient surface anatomy. The main advantage of photogrammetric scanning is that models can be rendered using photographs captured via smartphones [3]–[9]. Scanning with smartphones is significantly cheaper than other medical imaging modalities [1], [2] and results in reliable and robust surface accuracy on par with existing clinical gold standard technologies [10], [11]. Unfortunately, photogrammetry workflows often require extensive image segmentation, at the expense of human operator time and effort, in order to render 3D models [1].

Segmentation is an important problem in medical imaging and involves separating regions of interest (ROIs) from the rest of an acquired image. Convolutional neural networks (CNNs) are regarded as the dominant state-of-the-art approach for medical image segmentation in applications requiring high-accuracy [12], [13]. Deep convolutional neural networks (DCNNs), such as DeepLabv3, are able achieve high IoU performance when classifying pixels and outperform other CNN architectures [14]. Using transfer learning, it is possible to fine-tune pre-trained deep neural networks with instances from the target domain [15]. Transfer learning is crucial to medical imaging because in many cases it is not possible to collect sufficient training data [12], [13], [15].

We hypothesize that automating image segmentation via DeepLabv3 then rendering the segmented images using photogrammetry could create an efficient processing pipeline for scanning amputated limbs with smartphones. Automatic segmentation of limb photographs would allow for more photographs to be taken during the scanning procedure thus increasing the sampling density. With these additional photographs, it would be possible to improve the coverage and accuracy of 3D models. Finally, segmentation could help correct for motion of the limb during the scanning procedure. These potential benefits would allow photogrammetric limb scanning to be used on a larger scale to reach more patients in the clinic and remotely via telemedicine.

## II. BACKGROUND

### A. Photogrammetry for Medical Imaging

In its simplest form, photogrammetry is the science of measuring size and shape of objects using images [16]. In this context, photogrammetry has been used extensively since the 1950's for medical imaging and measurement [17]. The development of digital cameras and the accompanying transition to digital photogrammetry has led to technologies for the reconstruction of 3D models using photogrammetric algorithms [18]. Digital photogrammetry has been used successfully to reconstruct patient anatomy in many medical contexts such as cranial deformation scanning [8], [9], [19], facial scanning [10], [11], [20], and amputated limb scanning [3], [5]–[7].

Two values for accuracy are commonly reported for photogrammetric models: Root Mean Squared Error (RMSE) and Mean Absolute Error (MAE). RMSE values will always be greater than or equal to MAE values and are more susceptible to outliers, but are recommended when errors are unbiased and follow a normal distribution [21]. Close range photogrammetric approaches have been proven to have accuracy comparable to clinical gold standard technologies [20].

Using an Artec Spider structured light scanner as a clinical "gold standard" reference, [10] found that photogrammetric reconstructions of facial scans using 80 images captured had RMSE accuracy values of  $1.3 \text{ mm} \pm 0.3 \text{ mm}$ . In a similar study, [11] achieved RMSE accuracy values of  $1.5 \text{ mm} \pm 0.4 \text{ mm}$  with 30 photographs on reconstructions of the external ear. Using spherical objects with known geometry as a reference, [4] was able to achieve an MAE accuracy of  $0.3 \text{ mm} \pm 0.2 \text{ mm}$  using 95 images with tie point aids. In later research, these authors were able to achieve similar accuracy while scanning infant skulls with MAE accuracy values of  $0.5 \text{ mm} \pm 0.4 \text{ mm}$  and 200 images [8].

While the accuracy of photogrammetry for anatomical scanning is very good, workflows involving photogrammetry require a great deal of human input often taking hours [1], [19]. For this reason, recent research has focused on various methods for automating photogrammetric workflows for anatomical scanning [3], [8]. Photogrammetric models are rendered following acquisition (not in real time) thus errors in the image acquisition stage may not become evident until after a patient is scanned and no longer present. Automated approaches have focused their attention on this acquisition stage to ensure completeness of the results [22] with recent advances incorporating machine learning for landmark detection [9].

Still, automation of photogrammetric image processing (specifically image segmentation) remains a large problem [1]. Automating this image segmentation step could dramatically increase the speed of photogrammetric workflows for medical imaging, improving the clinical viability.

### B. Image Segmentation with Deep Learning

Medical image segmentation plays an essential role in modern clinical practice by facilitating computer aided diagnoses and making patient anatomical structures clear [13]. Prior to recent developments in deep learning (DL), computer vision techniques such as k-nearest neighbors (kNN), decision trees

(DT), support vector machines (SVM), and random forest (RF) models were utilized for segmentation and classification tasks [23] [24]. DL has superseded all of these approaches in medical imaging for several reasons, but most notably because the burden of feature engineering in DL shifts from humans to computers [25].

CNNs are the most heavily researched DL architectures for medical image analysis [26]. CNN architectures are composed of several fundamental building blocks: Convolution Layers, Pooling Layers, Activation Functions, Fully Connected Layers, and Loss Functions [27]. Convolution Layers are the most significant portion of CNNs and comprise a collection of convolutional filters (referred to as kernels). Input images are convolved using these filters to create an output feature map. Pooling Layers sub-sample the feature maps effectively shrinking them to create smaller feature maps. They also enlarge the receptive fields of neurons in subsequent layers allowing for translation invariance of the architecture. Activation Functions introduce non-linearity into the neural network and map inputs to outputs by selectively choosing to fire neurons. Fully Connected Layers are typically located at the end of the CNN architecture, with inputs from the final convolution or pooling layer, and are used as the CNN classifier. Loss functions are typically utilized in the output layer to calculate the predicted error across training samples [27]–[29].

The DeepLabv3 architecture expands on traditional CNNs by utilizing atrous convolution with spatial pyramid pooling [14]. Atrous convolution utilizes a dilated convolution kernel that, rather than focusing on adjacent pixels, convolves pixels that are not immediate neighbors. Atrous convolution helps to resolve the issue of spatial resolution loss in feature maps from successive convolution and de-convolution steps by allowing for precise control of feature map density. Atrous Spatial Pyramid Pooling (ASPP) [30] utilizes four parallel atrous convolutions with different atrous rates to transform feature maps. This allows for accurate and efficient classification regions at arbitrary scales [14]. These elements of the DeepLabv3 architecture result in better classification of pixels for semantic image segmentation, on par with other state-of-the-art models.

CNNs are prepared for medical imaging tasks via three major techniques: 1) Training CNNs from scratch using large datasets of labeled images. 2) Using "off-the-shelf" features without retraining the CNN to complement hand crafted features. 3) Pre-training the CNN on natural or medical images, then fine-tuning on target images (i.e. transfer learning) [31]. Transfer learning is commonly used to reduce the computational time and cost of training a neural network from scratch [13], [24], [25]. In medical imaging tasks, transfer learning has been shown to be as good as training CNNs from scratch and better in many cases [31], [32]. Recent research has shown great success in using transfer learning with the DeepLabv3 architecture for medical imaging segmentation [33].

## III. METHODS

### A. Transfer Learning using DeepLabv3

We performed transfer learning on a pre-trained resnet-101 based DeepLabv3 model downloaded from the Pytorch Model

Zoo [34]. This model was pre-trained on the COCO train2017 data set comprising 200,000 images and 80 object categories [35]. Our fine-tuning dataset consisted of 806 manually labeled images of limbs with transtibial amputations. This data was not augmented. These photographs were taken in a variety of conditions (e.g. different angles, indoor, outdoor, bare skin, with liners etc.). Images were downsampled from 3072 x 4096 to 300 x 400. Following this, we randomly select 80% of the images as our training data set and reserve the remaining 20% for validation.

We used Google Colab for training the model with dynamically scaled computer resources. In terms of the hyperparameters in fine-tuning, we used the Adam algorithm [36] for optimizing the parameters (e.g. weights) in the neural network with the default learning rate being set to  $10^{-5}$ . We employed the pixel-wise Mean Squared Error (MSE) as our loss function. We trained our fine-tuned neural network for 10 epochs using a batch size of 8 within each epoch.

### B. Scanning Workflow



**Fig. 1.** Scanning a Transtibial Amputee using the Lim(b)itless Cell Phone Application

We captured 24 limb scans to test the applicability of the neural network model for image segmentation. 12 scans were performed with a single transtibial amputee wearing a standard liner then 12 additional scans were performed with the transtibial amputee wearing a colored sock over their standard liner. Scans were performed utilizing the Lim(b)itless smartphone application [3] on a Motorola Moto G7 (MSRP \$299, Camera - 12 MP, f/1.8, 1/2.8") see Fig. 1.

The scanning procedure involved making two revolutions (one clockwise, one counterclockwise) around the outside of the limb while keeping the limb in frame of the application. Scans were taken at a constant radius of 30 cm from the limb, similar to [4], at a rotation rate of two revolutions per minute. This application automatically initiates a capture sequence at 10 degree intervals with each capture sequence including a burst of 3 photographs. For two full revolutions, this captures a hyper-redundant 216 images (minimum) per scan as recommended by [8]. Actual scanning time averaged  $52.4 \pm 6.1$  s while the actual number of images captured averaged  $287 \pm 29$ , Table I.

**TABLE I**  
IMAGE ACQUISITION AND RENDERING PIPELINE STATISTICS FOR SMARTPHONE SCANS (N = 22) USED IN THIS STUDY.

<b>Number of Images</b>	$287 \pm 29$
<b>Scan Time (s)</b>	$52.4 \pm 6.1$
<b>Segmentation Time (s)</b>	$890 \pm 111$
<b>Render Time (s)</b>	$3430 \pm 850$
<b>Scan Rate (images/s)</b>	$5.54 \pm 0.74$
<b>Segmentation Rate (images/s)</b>	$0.32 \pm 0.01$
<b>Render Rate (images/s)</b>	$0.088 \pm 0.022$

### C. Rendering Procedure

All segmentation and rendering was performed on a desktop server running an Intel(R) Xeon(R) CPU E5-1607 v3 3.10 GHz, Nvidia Quadro k2200 4 GB DDR5, and 256 GB DDR4 RAM 1866 MHz. Of the 24 limb scans acquired in the previous step, two scans were manually segmented via Adobe Photoshop and set aside as ground truth references. The remaining 22 scans, totaling 6312 images, were fed into the fine-tuned neural network for segmentation. Segmentation time using the neural network averaged  $890 \pm 111$  s, Table I.

3D limb models were rendered from these segmented images using Agisoft Metashape, Fig. 2. Agisoft is the most commonly used photogrammetric software in medical imaging being used by [3], [4], [10], [11], [19]. This step of the workflow was automated with no manual tie point alignment or point cloud segmentation. The resulting STL meshes were not smoothed prior to export, unlike [10], [11], [20]. This Laplacian smoothing step was foregone to evaluate the impact of segmentation method on model rendering.

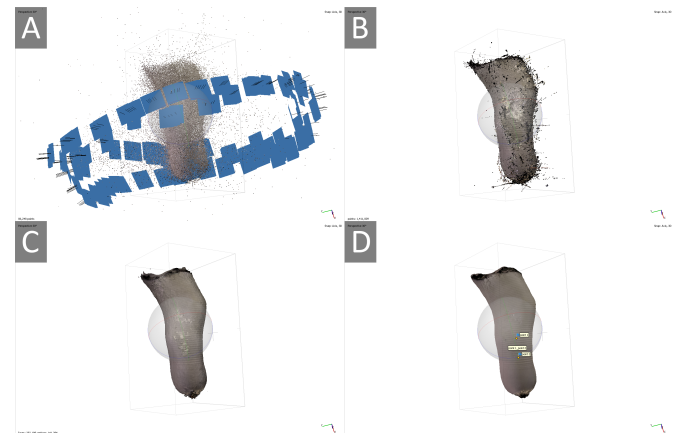


**Fig. 2.** Procedure for rendering limbs in Agisoft Metashape: A) Photo alignment and tie point detection. B) Creation of a dense point cloud. C) Conversion of point cloud to STL mesh. D) UV texture mapping and model scaling.

Finally, STL meshes of the scans rendered from automatically segmented images were compared with scans rendered from ground truth images via the CloudCompare open source 3D point cloud and mesh processing software. All limbs were cropped to the same boundaries, and outliers (visualized as extraneous floating points) were filtered out consistent with the technique used by [20]. Meshes were compared point by point via the cloud-to-mesh (C2M) measurement tool, with ground truth models being set as a reference.

## IV. RESULTS AND DISCUSSION

### A. Segmentation via Transfer Learning

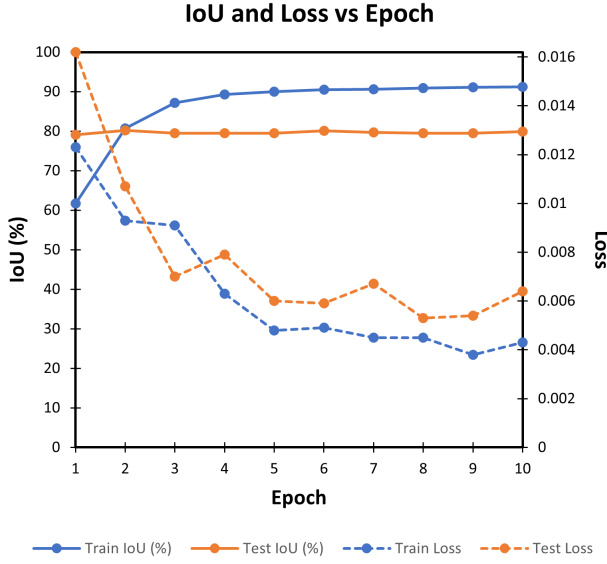


Fig. 3. Evolution of IoU and loss function for training and testing dataset

TABLE II  
TRAINING AND TESTING IOU METRICS AND LOSS FUNCTION  
EVOLUTION OVER THE COURSE OF TRANSFER LEARNING.

Epoch	Train IoU (%)	Test IoU (%)	Train Loss	Test Loss
1	61.7	79.1	0.0123	0.0162
2	80.7	80.2	0.0093	0.0107
3	87.2	79.5	0.0091	0.0070
4	89.3	79.5	0.0063	0.0079
5	90.0	79.5	0.0048	0.0060
6	90.5	80.1	0.0049	0.0059
7	90.6	79.7	0.0045	0.0067
8	90.9	79.5	0.0045	0.0053
9	91.1	79.5	0.0038	0.0054
<b>10</b>	<b>91.2</b>	<b>79.9</b>	<b>0.0043</b>	<b>0.0064</b>

Fig. 3 and Table II show the evolution of the fine tuned neural network over the transfer learning process. After 10 epochs of training, the fine tuned neural network showed excellent performance in segmenting images of transtibial amputations, see Fig. 4.

Looking at the training IoU curve, it can be observed that the training IoU performance increases with model epochs. This is to be expected as the training loss curve simultaneously decreases, reaching a local minimum at epoch 9. The descent rate of the loss function gradually slows as the number of epochs increases. Given this observation, training the model past 10 epochs would likely lead to over-fitting.

The testing loss function mirrors the training loss, reaching a local minimum at epoch 8. However, the testing IoU remains largely constant, with a value of 79.9% after 10 epochs of training. This IoU is comparable with values reported by [14] which reached peak mIoU values of 81.3% on the Cityscapes test set and 85.7% on the PASCAL VOC 2012 test set with the DeepLabv3 architecture.

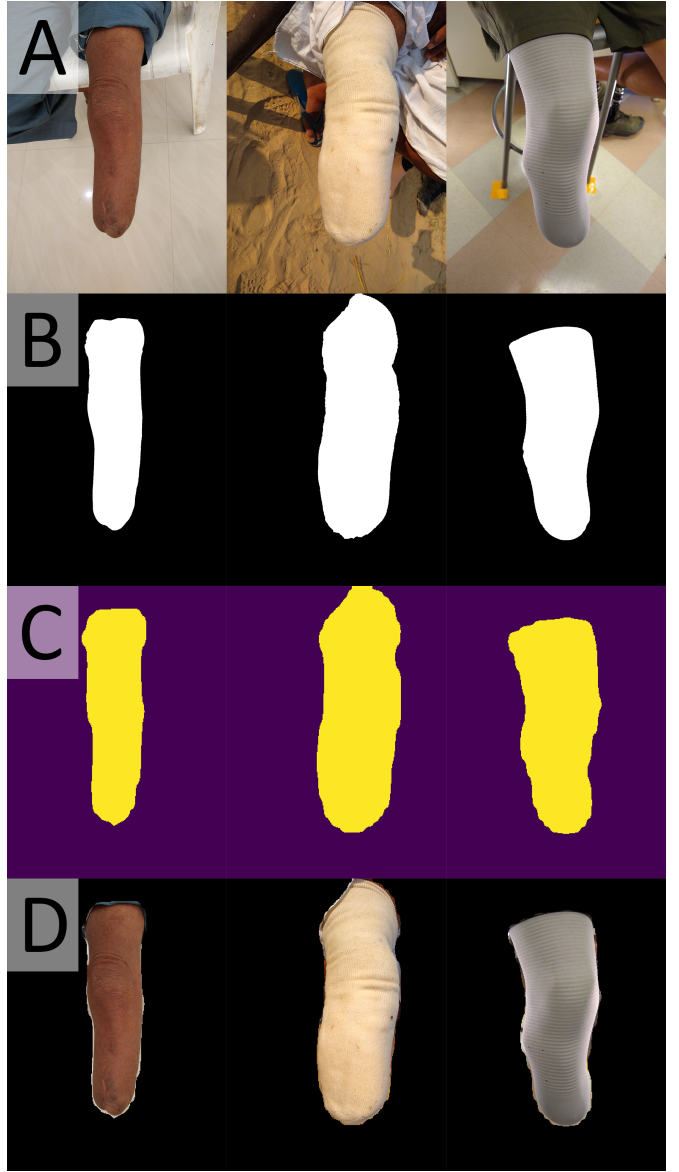


Fig. 4. Limbs with transtibial amputations used in the transfer learning process. A) These limb photographs were taken in a variety of lighting conditions and with different liners. B) Manually segmented binary masks representing the ground truth. C) Masks generated by the fine-tuned neural network. D) Applying the masks from the fine-tuned neural network to the original images.

The testing IoU value reported here could be improved in two ways: 1) Increasing the number of images in the labeled dataset 2) Reducing image downsampling. Increasing the number of images in the training dataset is feasible, but would require scanning additional persons with limb loss and manual segmentation. As with other forms of medical imaging, limited data quantities and expert annotations present hurdles for deep learning techniques [37]. On the other hand, reducing the image downsampling could improve the model performance without requiring additional annotations. In Fig. 4 it can be observed that the masks generated by the neural network are partially limited in accuracy due to this downsampling. Still any reduction in downsampling would likely be accompanied by an increased computational cost.

## B. Photogrammetry of Segmented Scans

TABLE III

SUMMARY OF CLOUD TO MESH (C2M) MEASUREMENT COUNT, MEAN ABSOLUTE ERROR (MAE) AND ROOT MEAN SQUARED ERROR (RMSE) OF 3D MODELS RENDERED AS PART OF THIS STUDY. MODELS WITH FAILED RENDERS FROM AUTOMATED WORKFLOW MARKED N/A.

All Scans	C2M Measurement Count	MAE (mm)	RMSE (mm)
Scan 1	149234	1.56	3.16
Scan 2	N/A	N/A	N/A
Scan 3	113706	0.06	1.26
Scan 4	86748	0.29	2.19
Scan 5	197356	0.28	2.16
Scan 6	104333	0.00	1.49
Scan 7	N/A	N/A	N/A
Scan 8	N/A	N/A	N/A
Scan 9	74548	0.25	4.32
Scan 10	110851	0.08	2.23
Scan 11	94102	0.05	1.58
Scan 12	118626	0.46	5.54
Scan 13	78901	0.17	1.26
Scan 14	N/A	N/A	N/A
Scan 15	73525	1.15	1.84
Scan 16	137258	0.06	3.31
Scan 17	134542	0.16	2.74
Scan 18	117213	0.01	1.76
Scan 19	66037	1.29	1.85
Scan 20	110057	1.44	2.19
Scan 21	65703	2.02	2.74
Scan 22	105424	0.93	2.13
Average	<b>107680 ± 33300</b>	<b>0.57 ± 0.63</b>	<b>2.43 ± 1.10</b>

Table III lists the Mean Absolute Error (MAE) and Root Mean Squared Error (RMSE) for the 22 limb scans rendered as part of this study. The average MAE values obtained are excellent ( $0.57 \text{ mm} \pm 0.63 \text{ mm}$ ) and comparable with the sub-millimeter MAE accuracy reported by [8]. The RMSE values are higher than those reported by [10], [11] with an average deviation of  $2.43 \text{ mm} \pm 1.10 \text{ mm}$ . Scans 1-11 using the bare liner had slightly better MAE and RMSE values ( $0.32 \text{ mm} \pm 0.51 \text{ mm}$ ;  $2.30 \text{ mm} \pm 1.01 \text{ mm}$ , respectively) than scans 12-22 with a colored sock over the bare liner ( $0.77 \text{ mm} \pm 0.70 \text{ mm}$ ;  $2.54 \text{ mm} \pm 1.21 \text{ mm}$ ). However the use of the colored sock improved tie point detection and image alignment leading to a successful render rate of 90.9 % for the colored sock vs 72.7% for the bare liner. Scans 2, 7, 8 and 14 did not render properly with the automated workflow. Failure was primarily due to failed photo alignment which led to incomplete and/or distorted models.

Looking at Fig. 5, it can be observed that the high RMSE values are primarily due to slight flexure of the limb between scans and not due to noise introduced by imperfect segmentation. Fig. 5B shows the CloudCompare results comparing Scan 12 to the ground truth. Scan 12 had a low MAE value (0.46 mm) but the highest RMSE value (5.54 mm) of all the scans. It is clear that high RMSE value is due to a change in limb geometry from flexure since the largest variations happen at the knee joint and at the distal end of the limb. This result was obtained even after controlling axis alignment and rotation of the models via the Iterative Closest Point (ICP) algorithm. This pattern is reflected in many other scans, see Fig. 5D and Fig. 5E.

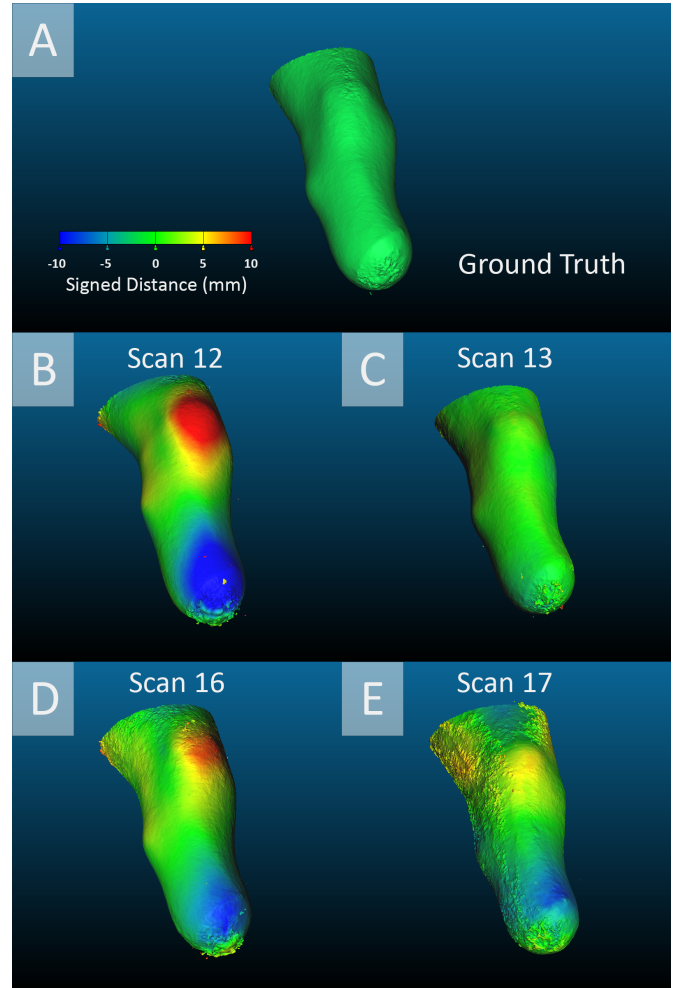


Fig. 5. Selected comparison of limbs in CloudCompare. In these 3D scans, it is evident that the large RMSE is due to a change in geometry from limb flexure, and is not due to segmentation or render quality. A) Ground truth model rendered from manually segmented images. B) Scan 12 - Highest RMSE (5.54 mm) evident limb flexure C) Scan 13 - Low RMSE (1.26 mm) no limb flexure D) Scan 16 - Medium RMSE (3.31 mm) evident limb flexure E) Scan 17 - Medium RMSE (2.71 mm) evident surface noise and limb flexure.

Poor surface finish, as evidenced by Fig. 5E, contributes far less to the MAE and RMSE values than flexure of the limb. This is important because poor surface finish can be directly tied to the quality of image segmentation, with better segmentation leading to smoother finishes. Although the accuracy is slightly diminished due to noise, it is not the main cause of error in these scans. Poor surface finish can be accounted for in practice by utilizing Laplacian smoothing functions. Fig. 5C is an example of a limb with low MAE (0.17 mm) and low RMSE (1.26 mm) values. Even without Laplacian smoothing, this model shows remarkable rendering accuracy in comparison with the ground truth.

Since the RMSE errors are systematically impacted by limb flexure, MAE is the more appropriate measure of accuracy in these scans. For the purposes of rendering residual limb models, sub-millimeter accuracy presents little meaningful advantage to clinicians and practitioners. Unlike the skulls studied by [8], [19], amputated limbs undergo constant shape

and deformation changes due to effects of donning-doffing, muscle contractions, interstitial fluid movements etc. [38], [39]. Traditional methods utilizing Plaster of Paris (PoP) casting as well as clinical gold standards utilizing MRI struggle with shape capture repeatability [40]. Clinicians account for at least a 5-9% volumetric variation in limb size and accommodate for it in socket design [38]. Given this context, variation in limb shape and size between scans is to be expected.

### C. Clinical Impact and Telemedicine Directions

The advances in photogrammetric limb scanning resulting from automation of the segmentation step could have potentially significant consequences. Notably, automatic segmentation decreases the amount of human time and effort required to render photogrammetric models. As mentioned previously in the methods, a limb scan captured via the Lim(b)itless smartphone application captures at least 216 images. Manual segmentation of those images would take (at minimum) 1 minute per image leading to a segmentation time of 12,960 seconds. The fine-tuned network trained in this paper would only take 675 seconds to perform this task based on the segmentation rate reported in Table I. This step is 19.2x faster and requires no human effort, demonstrating a remarkable increase in performance. Evaluating the end to end process using the rate values in Table I reveals that the model rendering workflow is 4.88x faster overall. Although the process bottleneck shifts from segmentation rate to rendering rate, the only step requiring significant human input is the scanning stage which takes less than 1 minute on average, Table I.

Models from the updated photogrammetric workflow could be used in a variety of contexts, since there was no significant geometrical difference between ground truth models and models rendered from images segmented by the fine-tuned neural network. Most notably, photogrammetric models built from smartphone scans can facilitate a host of low-cost telemedicine solutions. As one example, the limb models could be utilized as the first stage of digital prosthetic socket rectification. This would enable patients to be able to be scanned outside of a clinical environment (eg. at home) and have a prosthesis fabricated digitally and shipped to them. Aside from this, one distinct advantage of the photogrammetric process is it retains surface features which can be reprojected onto the final 3D model. With UV texture mapping, doctors could get a 3D view of limbs and look closely at their outer surfaces (such as for lesions) in virtual reality (VR). Photogrammetric limb scanning could also facilitate long-term and large scale studies of limb shape and size fluctuations over time. Being able to capture data outside of a clinical environment could help clinicians to increase the number of data points and the frequency of measurements beyond what is currently possible.

Several limitations would need to be overcome before using this technology at scale. On a technical level, the fine-tuned segmentation model from this research would need to be evaluated for robustness. Obtaining more scans of different skin colors, different lighting environments, etc. while training the model further could improve the robustness and reduce the risk of bias. It remains to be seen whether this model

could be applied to segment different types of amputation or if the model would need to be trained on additional examples. Finally, as noted in [2], privacy and regulatory requirements will be the largest concern in implementing a telemedicine system at scale utilizing smartphone photogrammetry. Any healthcare solution would need to comply with the appropriate regulatory guidelines for telemedicine.

## V. CONCLUSION

This research sought to address limitations in photogrammetric workflows by automating image segmentation via a fine-tuned deep learning model. Some important conclusions are summarized here:

- After 10 epochs of transfer learning, the fine-tuned deep learning model was able to achieve an IoU of 79.9% on the testing training set. The model's loss function indicated that it had reached a local minimum, thus the IoU could not be improved without the risk of overfitting. IoU could be improved by increasing the number of labeled training examples which could also increase model robustness.
- Applying this fine-tuned model to segment a dataset of 22 scans containing 6312 images showed that there was no significant geometric difference compared to scans rendered from manually segmented images. The MAE was found to be on average  $0.57 \text{ mm} \pm 0.63 \text{ mm}$  while the RMSE was found to be on average  $2.43 \text{ mm} \pm 1.10 \text{ mm}$ . The error reported was mostly influenced by slight changes in limb shape between scans and not render noise caused by image segmentation.
- Using the fine-tuned model increased the rate of image segmentation by 19.2x as well as sped up the entire photogrammetric workflow by a factor of 4.88x. This performance increase is remarkable since the step requiring the largest human effort was completely automated.
- This fine-tuned deep learning model can help facilitate large scale image processing for telemedicine applications. Using smartphones to acquire 3D scans of amputated limbs, clinicians could monitor patients, conduct large scale research studies, and even build prostheses remotely. This could potentially increase the standard of care for persons with limb loss who do not live near a clinic by matching patients with clinicians seeking to expand their geographic service area.

## ACKNOWLEDGMENT

The authors would like to give a special thanks to the generous support from the Center for Human Frontiers and the Qualcomm Institute at UC San Diego for providing facilities for this research project. In addition, the authors appreciate Bhagwan Mahaveer Viklang Sahayata Samiti (Jaipur Foot) for generously sharing their knowledge of prosthetic manufacturing technology and aiding in data collection. Finally, the authors would like to thank all of the other students involved on the Project Lim(b)itless team for their incredible support and positive energy which led to the successful completion of this research.

## REFERENCES

- [1] I. A. Cabrera, T. C. Pike, J. M. McKittrick, M. A. Meyers, R. R. Rao, and A. Y. Lin, "Digital healthcare technologies: Modern tools to transform prosthetic care," *Expert Review of Medical Devices*, pp. 1–16, Oct. 2021. [Online]. Available: <https://www.tandfonline.com/doi/full/10.1080/17434440.2021.1991309>
- [2] N. C. Paxton, R. C. Nightingale, and M. A. Woodruff, "Capturing patient anatomy for designing and manufacturing personalized prostheses," *Current Opinion in Biotechnology*, vol. 73, pp. 282–289, Feb. 2022. [Online]. Available: <https://linkinghub.elsevier.com/retrieve/pii/S0958166921001695>
- [3] I. A. Cabrera, Z. Zheng, P. Castillo, E. Ngo, S. Troncoso, W.-Y. Zhao, N. Sheth, C. Gean, J. Hsiao, J. V. Laxa, J. Martin, M. A. Meyers, J. M. McKittrick, R. R. Rao, and A. Y. Lin, "Smartphone Telemedicine: A Novel Workflow for Creating Prosthetic Sockets Using Semi-automated Photogrammetry," preprint, Jul. 2020. [Online]. Available: <https://doi.org/10.36227/techrxiv.12704984.v1>
- [4] I. Barbero-García, M. Cabrelles, J. L. Lerma, and Marqués-Mateu, "Smartphone-based close-range photogrammetric assessment of spherical objects," *The Photogrammetric Record*, vol. 33, no. 162, pp. 283–299, Jun. 2018, publisher: John Wiley & Sons, Ltd. [Online]. Available: <https://doi.org/10.1111/phor.12243>
- [5] L. G. De Vivo Nicoloso, J. Pelz, H. Barrack, and F. Kuester, "Towards 3D printing of a monocoque transtibial prosthesis using a bio-inspired design workflow," *Rapid Prototyping Journal*, vol. 27, no. 11, pp. 67–80, Jan. 2021, publisher: Emerald Publishing Limited. [Online]. Available: <https://doi.org/10.1108/RPJ-06-2021-0136>
- [6] R. B. Taqriban, R. Ismail, M. Ariyanto, and A. F. Yaya Syah Putra, "3D Model of Photogrammetry Technique for Transtibial Prosthetic Socket Design Development," in *2019 International Seminar on Research of Information Technology and Intelligent Systems (ISRITI)*, Dec. 2019, pp. 456–461, journal Abbreviation: 2019 International Seminar on Research of Information Technology and Intelligent Systems (ISRITI).
- [7] R. Ismail, R. B. Taqriban, M. Ariyanto, A. T. Atmaja, Sugiyanto, W. Caesarendra, A. Glowacz, M. Irfan, and W. Glowacz, "Affordable and Faster Transradial Prosthetic Socket Production Using Photogrammetry and 3D Printing," *Electronics*, vol. 9, no. 9, 2020.
- [8] I. Barbero-García, J. L. Lerma, and G. Mora-Navarro, "Fully automatic smartphone-based photogrammetric 3D modelling of infant's heads for cranial deformation analysis," *ISPRS Journal of Photogrammetry and Remote Sensing*, vol. 166, pp. 268–277, Aug. 2020. [Online]. Available: <https://www.sciencedirect.com/science/article/pii/S0924271620301714>
- [9] I. Barbero-García, R. Pierdicca, M. Paolanti, A. Felicetti, and J. L. Lerma, "Combining machine learning and close-range photogrammetry for infant's head 3D measurement: A smartphone-based solution," *Measurement*, vol. 182, p. 109686, Sep. 2021. [Online]. Available: <https://www.sciencedirect.com/science/article/pii/S0263224121006527>
- [10] R. C. Nightingale, M. T. Ross, M. C. Allenby, M. A. Woodruff, and S. K. Powell, "A Method for Economical Smartphone-Based Clinical 3D Facial Scanning," *Journal of Prosthodontics*, vol. 29, no. 9, pp. 818–825, Dec. 2020, publisher: John Wiley & Sons, Ltd. [Online]. Available: <https://doi.org/10.1111/jopr.13274>
- [11] R. C. Nightingale, M. T. Ross, R. L. Cruz, M. C. Allenby, S. K. Powell, and M. A. Woodruff, "Frugal 3D scanning using smartphones provides an accessible framework for capturing the external ear," *Journal of Plastic, Reconstructive & Aesthetic Surgery*, vol. 74, no. 11, pp. 3066–3072, Nov. 2021. [Online]. Available: <https://www.sciencedirect.com/science/article/pii/S1748681521002382>
- [12] A. Kumar, L. Bi, J. Kim, and D. D. Feng, "Machine learning in medical imaging," in *Biomedical Information Technology*. Elsevier, 2020, pp. 167–196. [Online]. Available: <https://linkinghub.elsevier.com/retrieve/pii/B9780128160343000055>
- [13] R. Wang, T. Lei, R. Cui, B. Zhang, H. Meng, and A. K. Nandi, "Medical Image Segmentation Using Deep Learning: A Survey," *IET Image Processing*, vol. 16, no. 5, pp. 1243–1267, Apr. 2022, arXiv: 2009.13120. [Online]. Available: <http://arxiv.org/abs/2009.13120>
- [14] L.-C. Chen, G. Papandreou, F. Schroff, and H. Adam, "Rethinking Atrous Convolution for Semantic Image Segmentation," *arXiv:1706.00587 [cs]*, Dec. 2017, arXiv: 1706.00587. [Online]. Available: <http://arxiv.org/abs/1706.00587>
- [15] F. Zhuang, Z. Qi, K. Duan, D. Xi, Y. Zhu, H. Zhu, H. Xiong, and Q. He, "A Comprehensive Survey on Transfer Learning," *arXiv:1911.02685 [cs, stat]*, Jun. 2020, arXiv: 1911.02685. [Online]. Available: <http://arxiv.org/abs/1911.02685>
- [16] J. Fryer, "1.1 Photogrammetry," in *Close Range Photogrammetry and Machine Vision*, K. B. Atkinson, Ed. Whittles Publishing, 1996, pp. 1–8. [Online]. Available: <https://app.knovel.com/hotlink/pdf/id:kt01131E33/close-range-photogrammetry/photogrammetry>
- [17] I. Newton and H. Mitchell, "11. Medical Photogrammetry," in *Close Range Photogrammetry and Machine Vision*, K. B. Atkinson, Ed. Whittles Publishing, 1996, pp. 303–328. [Online]. Available: <https://app.knovel.com/hotlink/pdf/id:kt01131LF6/close-range-photogrammetry/medical-photogrammetry>
- [18] W. Linder, *Digital Photogrammetry: A Practical Course*, 4th ed. Berlin, Heidelberg: Springer Berlin Heidelberg : Imprint: Springer, 2016.
- [19] I. Barbero-García, J. L. Lerma, Marqués-Mateu, and P. Miranda, "Low-Cost Smartphone-Based Photogrammetry for the Analysis of Cranial Deformation in Infants," *World Neurosurgery*, vol. 102, pp. 545–554, Jun. 2017. [Online]. Available: <https://linkinghub.elsevier.com/retrieve/pii/S1878875017303273>
- [20] M. T. Ross, R. Cruz, T. L. Brooks-Richards, L. M. Hafner, S. K. Powell, and M. A. Woodruff, "Comparison of three-dimensional surface scanning techniques for capturing the external ear," *Virtual and Physical Prototyping*, vol. 13, no. 4, pp. 255–265, 2018, publisher: Taylor & Francis .eprint: <https://doi.org/10.1080/17452759.2018.1493803>. [Online]. Available: <https://doi.org/10.1080/17452759.2018.1493803>
- [21] T. Chai and R. R. Draxler, "Root mean square error (RMSE) or mean absolute error (MAE)? – Arguments against avoiding RMSE in the literature," *Geoscientific Model Development*, vol. 7, no. 3, pp. 1247–1250, Jun. 2014. [Online]. Available: <https://gmd.copernicus.org/articles/7/1247/2014/>
- [22] E. Nocerino, F. Poiesi, A. Locher, Y. T. Tefera, F. Remondino, P. Chippindale, and L. Van Gool, "3D RECONSTRUCTION WITH A COLLABORATIVE APPROACH BASED ON SMARTPHONES AND A CLOUD-BASED SERVER," *The International Archives of the Photogrammetry, Remote Sensing and Spatial Information Sciences*, vol. XLII-2/W8, pp. 187–194, 2017. [Online]. Available: <https://www.int-arch-photogramm-remote-sens-spatial-inf-sci.net/XLII-2-W8/187/2017/>
- [23] P. Thanh Noi and M. Kappas, "Comparison of Random Forest, k-Nearest Neighbor, and Support Vector Machine Classifiers for Land Cover Classification Using Sentinel-2 Imagery," *Sensors*, vol. 18, no. 2, p. 18, Dec. 2017. [Online]. Available: <http://www.mdpi.com/1424-8220/18/1/18>
- [24] N. O. Mahony, S. Campbell, A. Carvalho, S. Harapanahalli, G. Velasco-Hernandez, L. Krpalkova, D. Riordan, and J. Walsh, "Deep Learning vs. Traditional Computer Vision," *arXiv:1910.13796 [cs]*, Oct. 2019, arXiv: 1910.13796. [Online]. Available: <http://arxiv.org/abs/1910.13796>
- [25] D. Shen, G. Wu, and H.-I. Suk, "Deep Learning in Medical Image Analysis," *Annual Review of Biomedical Engineering*, vol. 19, no. 1, pp. 221–248, Jun. 2017, publisher: Annual Reviews. [Online]. Available: <https://doi.org/10.1146/annurev-bioeng-071516-044442>
- [26] J. Ker, L. Wang, J. Rao, and T. Lim, "Deep Learning Applications in Medical Image Analysis," *IEEE Access*, vol. 6, pp. 9375–9389, 2018.
- [27] L. Alzubaidi, J. Zhang, A. J. Humaidi, A. Al-Dujaili, Y. Duan, O. Al-Shamma, J. Santamaría, M. A. Fadhel, M. Al-Amidie, and L. Farhan, "Review of deep learning: concepts, CNN architectures, challenges, applications, future directions," *Journal of Big Data*, vol. 8, no. 1, p. 53, Dec. 2021. [Online]. Available: <https://journalofbigdata.springeropen.com/articles/10.1186/s40537-021-00444-8>
- [28] I. Goodfellow, Y. Bengio, and A. Courville, *Deep learning*, ser. Adaptive computation and machine learning. Cambridge, Massachusetts: The MIT Press, 2016.
- [29] T. M. Arif, *Introduction to deep learning for engineers: using Python and Google Cloud Platform*, 2020, oCLC: 1181834611. [Online]. Available: <http://public.eblib.com/choice/PublicFullRecord.aspx?p=6273049>
- [30] L.-C. Chen, G. Papandreou, I. Kokkinos, K. Murphy, and A. L. Yuille, "DeepLab: Semantic Image Segmentation with Deep Convolutional Nets, Atrous Convolution, and Fully Connected CRFs," *arXiv:1606.00915 [cs]*, May 2017, arXiv: 1606.00915. [Online]. Available: <http://arxiv.org/abs/1606.00915>
- [31] H.-C. Shin, H. R. Roth, M. Gao, L. Lu, Z. Xu, I. Nogues, J. Yao, D. Mollura, and R. M. Summers, "Deep Convolutional Neural Networks for Computer-Aided Detection: CNN Architectures, Dataset Characteristics and Transfer Learning," *IEEE Transactions on Medical Imaging*, vol. 35, no. 5, pp. 1285–1298, May 2016. [Online]. Available: <https://ieeexplore.ieee.org/document/7404017/>
- [32] N. Tajbakhsh, J. Y. Shin, S. R. Gurudu, R. T. Hurst, C. B. Kendall, M. B. Gotway, and J. Liang, "Convolutional Neural Networks for Medical Image Analysis: Full Training or Fine Tuning?" *IEEE*

- Transactions on Medical Imaging*, vol. 35, no. 5, pp. 1299–1312, May 2016. [Online]. Available: <http://ieeexplore.ieee.org/document/7426826/>
- [33] S. Roy, W. Menapace, S. Oei, B. Luijten, E. Fini, C. Saltoni, I. Huijben, N. Chennakeshava, F. Mento, A. Sentelli, E. Peschiera, R. Trevisan, G. Maschietto, E. Torri, R. Inchegolo, A. Smargiassi, G. Soldati, P. Rota, A. Passerini, R. J. G. van Sloun, E. Ricci, and L. Demi, “Deep Learning for Classification and Localization of COVID-19 Markers in Point-of-Care Lung Ultrasound,” *IEEE Transactions on Medical Imaging*, vol. 39, no. 8, pp. 2676–2687, Aug. 2020. [Online]. Available: <https://ieeexplore.ieee.org/document/9093068/>
- [34] A. Paszke, S. Gross, F. Massa, A. Lerer, J. Bradbury, G. Chanan, T. Killeen, Z. Lin, N. Gimelshein, L. Antiga, A. Desmaison, A. Kopf, E. Yang, Z. DeVito, M. Raison, A. Tejani, S. Chilamkurthy, B. Steiner, L. Fang, J. Bai, and S. Chintala, “Pytorch: An imperative style, high-performance deep learning library,” in *Advances in Neural Information Processing Systems 32*, H. Wallach, H. Larochelle, A. Beygelzimer, F. d’Alché-Buc, E. Fox, and R. Garnett, Eds. Curran Associates, Inc., 2019, pp. 8024–8035. [Online]. Available: <http://papers.neurips.cc/paper/9015-pytorch-an-imperative-style-high-performance-deep-learning-library.pdf>
- [35] T.-Y. Lin, M. Maire, S. Belongie, L. Bourdev, R. Girshick, J. Hays, P. Perona, D. Ramanan, C. L. Zitnick, and P. Dollár, “Microsoft COCO: Common Objects in Context,” *arXiv:1405.0312 [cs]*, Feb. 2015, arXiv: 1405.0312. [Online]. Available: <http://arxiv.org/abs/1405.0312>
- [36] D. P. Kingma and J. Ba, “Adam: A Method for Stochastic Optimization,” *arXiv:1412.6980 [cs]*, Jan. 2017, arXiv: 1412.6980. [Online]. Available: <http://arxiv.org/abs/1412.6980>
- [37] G. Wang, W. Li, M. A. Zuluaga, R. Pratt, P. A. Patel, M. Aertsen, T. Doel, A. L. David, J. Deprest, S. Ourselin, and T. Vercauteren, “Interactive Medical Image Segmentation Using Deep Learning With Image-Specific Fine Tuning,” *IEEE Transactions on Medical Imaging*, vol. 37, no. 7, pp. 1562–1573, Jul. 2018. [Online]. Available: <https://ieeexplore.ieee.org/document/8270673/>
- [38] E. Suyi Yang, N. Aslani, and A. McGarry, “Influences and trends of various shape-capture methods on outcomes in trans-tibial prosthetics: A systematic review,” *Prosthetics & Orthotics International*, vol. 43, no. 5, pp. 540–555, Oct. 2019. [Online]. Available: <https://journals.lww.com/10.1177/0309364619865424>
- [39] D. Solav, K. M. Moerman, A. M. Jaeger, and H. M. Herr, “A Framework for Measuring the Time-Varying Shape and Full-Field Deformation of Residual Limbs Using 3-D Digital Image Correlation,” *IEEE Transactions on Biomedical Engineering*, vol. 66, no. 10, pp. 2740–2752, Oct. 2019. [Online]. Available: <https://ieeexplore.ieee.org/document/8625546/>
- [40] M. R. Safari, P. Rowe, A. McFadyen, and A. Buis, “Hands-Off and Hands-On Casting Consistency of Amputee below Knee Sockets Using Magnetic Resonance Imaging,” *The Scientific World Journal*, vol. 2013, p. 486146, Nov. 2013, publisher: Hindawi Publishing Corporation. [Online]. Available: <https://doi.org/10.1155/2013/486146>